Force reconstruction

from tapping mode force microscopy experiments

Amir F. Payam, Daniel Martin-Jimenez, Ricardo Garcia*

Instituto de Ciencia de Materiales de Madrid, CSIC

Sor Juana Inés de la Cruz 3

28049 Madrid, Spain

* Electronic address: r.garcia@csic.es

Fast, accurate and robust nanomechanical measurements are intensely searched in materials science, applied physics and molecular biology. Amplitude modulation force microscopy (tapping mode) is the most established nanoscale characterization technique of surfaces for air and liquid environments. However, its quantitative capabilities lag behind its high spatial resolution and robustness. We develop a general method to transform the observables into quantitative force measurements. The force reconstruction algorithm has been deduced on the assumption that the observables (amplitude and phase shift) are slowly varying functions of the tip-surface separation. The accuracy and applicability of the method is validated by numerical simulations and experiments. The method is valid for liquid and air environments, small and large free amplitudes, compliant and rigid materials, conservative and non-conservative forces.

I. INTRODUCTION

The evolution of force microscopy (AFM) [1] is shaped by the transition from a high spatial resolution technique [2-7] to a method that provides spatially resolved maps of mechanical or chemical properties [8-15]. Those maps have found applications in life sciences to understand the relationship between protein flexibility and biological function [14-16]; polymer sciences to develop novel ultra-thin polymer blends [17] or in biomedicine as a finger-prints of malignant cells and tissues [18]. The mechanical and chemical properties are deduced from the force-distance curves. The standard approach to obtain a force-distance curve uses the static AFM configuration. This approach requires recording the dependence of the cantilever deflection versus the tip-surface distance for the different (x, y) positions of the surface [14-19]. This approach measures forces in quasi-static equilibrium, consequently only conservative or adhesion hysteresis forces can be measured.

Tapping mode AFM, also known as amplitude modulation AFM (AM-AFM), remains the most widely used method for nanoscale characterization of surfaces in air and liquid [3, 20]. Furthermore, high speed in combination with high resolution imaging has been implemented by incorporating, among other advances, a feedback loop in the amplitude [4, 5]. AM-AFM has been very successful in providing compositional contrast images of heterogeneous surfaces and measuring energy dissipation [21, 22], however, the technique does not provide the interaction force. Consequently, it cannot directly measure properties such as the stiffness, the elastic modulus or the viscoelastic coefficient [23]. This is in contrast with frequency modulation AFM, where its ability to recover the interaction force has been established more than ten years ago [24, 25].

In fact, several aspects of AM-AFM are still under development, in particular, the transformation of observables into quantitative force measurements [26-31] or the tip wear during imaging [32]. In dynamic AFM experiments the forces are not direct observables because the observables are averaged over one or several oscillation cycles [20, 33]. As a consequence the observables are provided as a function of the probe-sample separation instead of the instantaneous tip-surface distance. The latter distance is the relevant one to determine the force curve.

The limitations of tapping mode AFM to determine the forces acting on the tip have fundamental and practical implications. They could point out the existence of an intrinsic limitation of the technique. It has been argued that the transition between attractive and repulsive interaction regimes [20] would prevent recovering the whole force curve [33]. On the other hand, the field of nanomechanical spectroscopy would be expanded and simplified if the force curve could also be obtained from tapping mode AFM experiments.

Let's first examine the attempts to recover the force in conventional AM-AFM (single frequency). Those methods can be broadly classified into two categories: (i). Methods that recover the time-varying force by measuring the time-varying deflection [34-37]. The data in these methods is recorded at a fixed probe-surface separation. (ii).

Methods that provide, for a given probe-surface separation, the force value at the closest tip-surface distance of the steady-state oscillation cycle [38-41]. Then the procedure is repeated for different probe-surface separation to obtain the whole force curve.

The methods of the first category rely on the determination of the higher harmonics and the cantilever transfer function. The accuracy of these approaches has a strong dependence on the number of harmonics. In general more than 20 harmonics are needed to render a satisfactory force reconstruction. In addition, the generation of harmonic components above the noise level is not compatible with high resolution imaging. Torsional harmonic AFM offers an alternative [37, 42, 43] to address the above issues although it requires to modify the instrument and the use of special cantilevers where the tip is offset from the main cantilever axis. The above methods reconstruct the force curve at a fixed probe-surface separation. The force reconstruction methods based on intermodulation excitation could also be included in the above category [26,27,44]. These methods are performed at a fixed probe-surface separation and require the measurement of several frequency components.

The methods of the second category start from the integral equations provided by the virial (in-phase) and energy balance (quadrature) equations [45]. To solve the integral equations involves several intermediate steps and approximations such as to express the force in terms of its inverse Laplace transform [39] or the expansion of the force in terms of Chebyshev polynomials of the first kind [40]. Both cases involve the determination of a large number of parameters which makes those approaches unpractical. Holscher's approach simplifies the integral equation by considering that the amplitudes in AM mode are larger than the interaction range of the tip-sample force [38,46] while Katan *et al*. method [41] is based on an *ad hoc* equivalence between frequency and amplitude modulation AFM observables that lacks a rigorous demonstration. Recently, Platz et *al.* introduced a force reconstruction method that incorporates some features of both categories [47].

Here we develop a force reconstruction method that is general because is valid for small and large amplitudes; operation in air and liquid; compliant and rigid materials, conservative and non-conservative interactions alike. The method is based on assuming that the amplitude and the phase shift of the oscillation are slowly varying functions of the probe-surface separation. For any probe-surface separation, the method assumes a sinusoidal steady-state solution. In addition, the tip motion retains is harmonic form (sinusoidal) during the variation of the probe-surface separation. The response of the tip to variations in the probe-surface separation and, consequently, to the interaction forces is reflected by the changes of the amplitude and the phase shift.

II. THEORY

The slowly varying approximation in combination with the virial-dissipation equations allows us to derive two integral equations with little restrictions on the dependence of the force with the distance. The integral equations are solved by using

several intermediate steps, namely the use of Laplace transforms [48], modified Bessel functions and fractional integrals and derivatives [49].

The analysis of amplitude modulation AFM requires being familiar with several distances and/or displacements. Figure 1 illustrates the definition of the tip deflection $z(t)$, the distance at the closest approach d which could either be positive or negative (indentation), the probe-surface separation z_c, the average tip deflection z_0 which could be positive (repulsive regime) or negative (attractive regime) [20]. We note that the probe-surface separation will coincide with the average tip-surface distance whenever z_0 is negligible with respect A.

The experimental implementation of the method requires the acquisition of the dependence of the amplitude and phase shift with respect to the tip-surface distance. These curves are called, respectively, amplitude (phase) curves. In this process, the tip oscillates as it is approached towards the surface (at a fixed lateral position) by the action of a piezo-ceramic (z-piezo) Δz. This causes a change in the probe-surface separation. The z-piezo displacement involves frequencies in the 1-10 Hz range while the tip oscillation happens in the 10-400 kHz range. Consequently, it is a good approximation to consider that at each position of the curve the tip has reached its steady-state solution.

The cantilever tip-system is modelled as a driven and dampen point-mass oscillator that is under the influence of conservative F_c and non-conservative F_{nc} forces.

$$\ddot{z} + \frac{\omega_0}{Q}\dot{z} + \omega_0^2 z = \frac{\omega_0^2 F_{ts}}{k} + \frac{\omega_0^2 F_d}{k} \tag{1}$$

$$F_{ts} = F_c + F_{nc} = F_c(z) + \Lambda(z)\dot{z} \tag{2}$$

we assume a steady-state solution given by

$$z = z_0 + A\cos(\omega t - \phi) \tag{3}$$

where A and ϕ are respectively the amplitude and the phase shift; ω_0 and ω are, respectively, the (angular) resonant and driving frequencies of the oscillator; k and Q are, respectively, the force constant and the quality factor of the cantilever-tip system; F_d is the driving force and z_0 is the average tip deflection; we assume that z_0 can be neglected with respect to A.

In the process of recording the amplitude and phase shift curves, we assume that the oscillation keeps the form given by equation (3) while both A and ϕ are slowly changing with time when the probe-surface separation goes from z_{c1} to z_{c2} in a time Δt. Let's also assume that the separation between z_{c1} and z_{c2} is much smaller than the amplitude A. The above hypothesis lead to

$$\dot{z} = \dot{A}\cos(\omega t - \phi) - A\omega \sin(\omega t - \phi) + A\dot{\phi}\sin(\omega t - \phi) = -A\omega \sin(\omega t - \phi) \quad (4)$$

$$\ddot{z} = -\dot{A}\omega \sin(\omega t - \phi) - A\omega^2 \cos(\omega t - \phi) + A\omega\dot{\phi}\cos(\omega t - \phi) \quad (5)$$

by introducing equations (4) and (5) into equation (1) and applying the virial and the energy balance considerations we obtain two integral equations. The virial theorem leads to an expression for the conservative force while the application of the energy balance over a period leads to an expression for the non-conservative forces.

$$F_c(d) = 2k\int_d^\infty X\,dx + 2k\int_d^\infty \frac{\alpha\sqrt{A}}{\sqrt{\pi(x-d)}}X\,dx - 2k\frac{\partial}{\partial d}\int_d^\infty \left(\frac{A^{3/2}}{\sqrt{2(x-d)}}X\right)dx \quad (6a)$$

$$F_c(d) \approx 2k\int_d^\infty X dx - 2k\frac{\partial}{\partial d}\int_d^\infty \left(\frac{A^{3/2}}{\sqrt{2(x-d)}}X\right)dx \quad (6b)$$

$$\Lambda(\mathrm{d}) = 2k\frac{\partial}{\partial d}\int_d^\infty Y dx + 2k\frac{\partial}{\partial d}\int_d^\infty \frac{\alpha\sqrt{A}}{\sqrt{\pi(x-d)}}Y dx - 2k\frac{\partial^2}{\partial d^2}\int_d^\infty \frac{A^{3/2}}{\sqrt{2(x-d)}}Y\,dx \quad (7a)$$

$$\Lambda(\mathrm{d}) \approx 2k\frac{\partial}{\partial d}\int_d^\infty Y dx - 2k\frac{\partial^2}{\partial d^2}\int_d^\infty \frac{A^{3/2}}{\sqrt{2(x-d)}}Y\,dx \quad (7b)$$

with

$$X = \frac{A_0}{2QA}\cos\phi - \frac{1}{2}\left(\frac{\omega_0^2-\omega^2}{\omega_0^2}\right) \quad (8)$$

$$Y = \frac{A_0}{2QA\omega}\sin\phi - \frac{1}{2Q\omega_0} \quad (9)$$

where A_0 is the free oscillation amplitude and $\alpha \approx 1/8$. The derivation of the simplified equations (6b) and (7b) will be explained below. The intermediate steps to deduce the above equations are explained in the Appendix.

Equations (6) and (7) provide, respectively, the conservative and non-conservative components of the force at the point of the oscillation where the tip is closest to the surface. For each *d* the input data are the *A* and ϕ. In each of the above equations, the right hand side is decomposed in three integrals. The meaning and relevance of those terms will be discussed in the next sections.

The method of slowly varying parameters has previously been used to calculate the average force [28], to derive an state-space model of a cantilever under feedback control [50] or to discuss high-resolution imaging with different feedback architectures [51].

III. METHODS

The accuracy of the method is analyzed by (1) using a tip-surface model force, (2) the model force is used to solve numerically equation of motion. This enables to determine A and ϕ as a function of the tip-surface separation. (3) The amplitude and phase shift curves deduced in step 2 are used as inputs in the equations (6) and (7) to reconstruct the force curve. Finally the force reconstructed from the theory is compared with the model force. On the other hand, the applicability of the theory is demonstrated by reconstructing the force from experimental data while its validity to measure nanomechanical data is tested against conventional and bimodal force spectroscopy measurements.

A. Simulations

The numerical solution of equation (1) was calculated by using a fourth-order Runge-Kutta algorithm. The simulations have been performed for two different cantilevers, one that applies for air and the other for measurements in water. The values used for the resonant frequency, force constant and quality factor of the cantilevers are, respectively, 300 kHz, 30 N/m and 300 (air) and 30 kHz, 1 N/m and 2 (liquid). For the tip-sample interaction we simulated four different tip-surface interfaces (cases I to IV) , characterized by the Young modulus E_s, Hamaker constant H and Poisson coefficient ν. Case I: E_s=10 GPa, H=10^{-19} J, ν=0.4 and R_{tip} = 2 nm. Case II: E_s=0.1 GPa, H=10^{-20} J and ν=0.35, R_{tip} = 5 nm. Case III: E_s=10 GPa, H=0 J, ν=0.4 and R_{tip} = 2 nm. Case IV: E_s=0.1 GPa, H=0 J, ν=0.35 and R_{tip} = 5 nm. To simulate dissipation in air we use E_s=100 MPa, H=0.5×10^{-20} J, ν=0.4, A_0=10 nm, η= 100 Pa.s and R_{tip} = 5 nm; in the liquid, E_s=100 MPa, H=0 J, ν=0.4, A_0=10 nm, η= 100 Pa.s and R_{tip} = 5 nm. For all the cases the tip was characterized by E_{tip}=160 GPa, ν=0.45. The intermolecular distance was set at 0.165 nm.

B. AFM measurements

The AFM data was acquired with a Cypher (Asylum Research Inc.). For air, we use PPP-NCLAuD cantilevers (Nanosensors) with Q= 440, k=22.4 N/m and the 1st resonant frequency f_0=150.418 kHz. For water, we use PPP-NCSTAuD cantilevers (Nanosensors) with Q= 5.4, k=6.5 N/m and f_0=60.41 kHz. The optical lever sensitivities were determined by acquiring static and dynamic curves on a stiff surface (mica) in the same medium as the experiments. The Q and f_0 were measured by using the thermal method at relatively close distances from the sample surface (~3 μm).

C. Polymer samples

The experiments have been performed on a polymer blend made of polystyrene (PS) regions (E_{PS}≈2.0 GPa) and polyolefin elastomer (ethylene-octene copolymer) regions (LDPE) (E_{LDPE}≈0.1 GPa). In both cases nominal values. The polymer blend is commercially available from Bruker (PS-LDPE-12M). The sample for liquid was a layer of Polystyrene (MW =13600 g/mol) on Silicon. The polymer was dissolved in

toluene (1wt %) and spin coated (1500 min^{-1}) onto a polished silicon(100) substrate, which was cleaned in three cycles with a solution of 1:1:2 in volume of Amonium Hydroxide(30%), Hydrogen Peroxide(30%) and pure water by ultrasonic treatment for 10 min each.

IV. RESULTS

Figures 2(a) and 2(d) show the amplitude and phase shift curves versus the z_c, respectively, for Q=300 (air) and Q=2 (water). Those curves have been obtained by modelling the tip-surface conservative force for a stiff surface E_s= 10 GPa (Case I and III, see Methods) and then solving the equation of motion. The amplitude shows a monotonic decrease with the probe-surface separation independent of the nature of the force while the shape of the phase shift curve is sensitive to the sign of the force (attractive versus repulsive). Panels 2(b) and 2(e) show the same data but now plotted with respect to the closest tip-surface distance. We observe that A and ϕ are multivalued functions of d. We also observe that A and ϕ changes are confined to a small range of tip-surface distances. In water, the long-range van der Waals force is screened which implies that the amplitude is reduced by short-range repulsive forces. The force curves are plotted in figures 2(c) (air) and 2(f) (water). The agreement between the actual interaction force used in the simulation and the force reconstructed from the amplitude and phase shift curves is remarkable. It is relevant to observe that in some circumstances the observables are multivalued functions of d . In those cases, the force reconstruction method could be still applied for d values that go from distances far from the sample to the minimum d value.

The method also enables to reconstruct the force curve on soft surfaces. To illustrate this we have performed some simulations for a material with a Young modulus of 100 MPa (Case II and IV, see Methods). Figure 3 shows the comparison between the actual and reconstructed force curve for both air and water environments. Again, there is a good agreement between the force of the model and the force reconstructed by using equation (6).

We have also calculated the relative error between the model force and the reconstructed force for different free amplitudes, oscillation amplitudes, tip-surface interaction regimes and sample material properties (Tables I to III). The relative error is below 5% for most common conditions. The error comes from several sources such as the deviation of the actual motion from a sinusoidal oscillation or in the determination of the dependence of A with amplitude ratio (y) that is needed to solve the integrals of equations (6) and (7).

In liquid (Table I) the relative error is below 5% in most of the cases. We observe that the error decreases with decreasing the free amplitude and it increases with decreasing A. For high Q values (air) the relative error in the repulsive regime is below 5% for the relevant operating range ($A \geq 0.8A_0$). In the attractive regime (Table III) the relative error is always rather small (below 2%).

TABLE I. Relative error in the force reconstruction (water)

$y=A/A_0$	E_s=100 MPa		E_s=10 GPa	
	A_0= 1 nm	A_0= 10 nm	A_0= 1 nm	A_0= 10 nm
1-0.9	1.1%	5%	0.4%	10%
0.89-0.8	3.6%	4%	0.4%	6%
0.799-0.7	4.5%	3%	2.1%	2%
0.699-0.6	12%	3%	12%	2%
0.599-0.5	17%	6%	16%	10%

TABLE II. Relative error in the force reconstruction in air (repulsive regime)

$y=A/A_0$	E_s=100 MPa		E_s=10 GPa	
	A_0= 10 nm	A_0= 50 nm	A_0= 10 nm	A_0= 50 nm
1-0.9	2%	1.4%	1.9%	6.1%
0.89-0.8	7%	2.7%	1.9%	3.9%
0.799-0.7	7%	12%	4.5%	2%
0.699-0.6	11%	15%	4.5%	11%
0.599-0.5	20%	25%	5.5%	12%

TABLE III. Relative error in the force reconstruction in air (attractive regime)

$y=A/A_0$	E_s=100 MPa		E_s=10 GPa	
	A_0= 10 nm	A_0= 50 nm	A_0= 10 nm	A_0= 50 nm
1-0.9	0.2%	1.0%	0.2%	2%

V. DISCUSSION

To understand the relative contributions of the three integrals presented on the right hand side of equation (6a) we plot them separately for simulations performed in air (A_0=10 nm, Q=300) and water (A_0=5 nm , Q=2). In both cases E_s=50 MPa. Figure 4(a) shows that for high Q values (air), the third integral is the dominant term in the force reconstruction process. Only at relative high indentations some very minor differences appear. For low Q environments (water) the force reconstruction curve carries contributions from the 1st and the 3rd integral. The 3rd term still dominates but the contribution from the 1st integral cannot be neglected. In all the cases, the 2nd integral gives negligible contributions. This happens because at large distances the prefactor in

the 2nd integral goes to zero. On the other hand, when the tip is close to the surface X goes to zero faster than the prefactor goes to infinity. Consequently, the force reconstruction algorithm becomes more compact with just two integrals (equation (6b)). The derivatives are very sensitive to small changes of the variable, then it is reasonable to find that the dominant term of the force reconstruction is the one that involves the partial derivative in the third integral.

We also compare the present method with the non-polynomial methods proposed to reconstruct the force [38, 41]. Figure 4(c) shows the force reconstruction obtained in air (Q=300). Four curves are shown, the model force, the force reconstructed by the present (reconstructed), Katan [41] and Holscher [33,38] methods. The method proposed here matches the model force and gives a good agreement with the model in the repulsive regime for all the range. We note that for stiffer surfaces the differences between the three reconstruction methods and model force decrease. Katan's overstimates the attractive region and underestimates the value of the force in the repulsive region. Holscher method provides a good approximation to the force curve in the attractive region. However, the force reconstruction does not cover the complete range of tip-surface separations. The method is not applied in the region where the tip jumps from the repulsive to the attractive regime.

In water (Fig. 4(d)) the force reconstruction matches the model for all the indentation range. This has also been verified by using other parameters in the simulations. Holscher method departs from the model force as the indentation increases. This happens because Holscher method is based on the assumption that the amplitude is larger than the indentation. This assumptions could fail on soft matter because the indentation could be comparable to the amplitude. Katan method offers a good agreement with the model. Only at high indentation some differences appear.

The force reconstruction method proposed also applies to recover non-conservative interactions. In particular, we analyse the case of a dissipative force proportional to the velocity. Two comparisons are performed (air and water) (Fig. 5). First we evaluate the relative contributions of the three terms shown in equation (7a). Similarly to the findings for the conservative forces, the method only requires contributions from the 1st and the 3rd integral. In both cases there is a very good agreement between the 'real' term and the reconstructed term. Some minor differences appear by increasing the indentation (Fig. 5(c),(d)). In liquid at 2 nm there is hardly any error and at 4 nm the relative error is about 10%.

Next we have applied the method to reconstruct the force from experiments performed on a polymer blend (Fig. 6(a)). The blend is made of two regions, a mildly stiff region (PS) of about 2 GPa that encloses moderately soft regions (LDPE) of about 100 MPa. Figure 6(b) shows the amplitude and phase shift curves obtained in air on a polystyrene region of the blend. The raw experimental data are recorded as a function of the z-piezo displacement (Δz). To express those curves in terms of the actual tip-surface

distance we use the following relationship between the minimum tip-surface distance d and the z-piezo displacement (Fig. 6(c))

$$z_c \approx \Delta z + distance\ offset \quad (10)$$

$$d = z_c + z_0 - A \quad (11)$$

When there is not an attractive regime, d=0 is taken at the position where the amplitude starts to decrease (A=0.99A_0). If there is an attractive regime, d=0 is taken at the position where the phase shift has a maximum (Fig. 6(c)). Figure 6(d) shows the amplitude and phase curves versus the distance. The presence of negative values indicates that the tip is indenting the material. Figure 6(e) shows the force reconstructed from the experimental data. The amplitude and phase shift curves show the presence of attractive and repulsive interaction regimes. Those regimes are reflected in the force curve that shows the presence of attractive and repulsive regions.

The strength of the attractive region is greatly decreased by performing the experiments in water. Figure 6(j)-(n) shows the results for an experiment performed on PS in water. The panels k-n illustrate the sequence to transform the observables into the force curve.

To validate the method we have also compared the values of the Young modulus deduced from the above force curves with the nominal values of the sample and with the values measured by conventional force spectroscopy and bimodal AFM [52-53]. In both cases there is a good agreement. In particular, for the PS we have obtained an effective Young modulus in the 1.5-2 GPa range (2 GPa nominal reference value) while for the LDPE we have obtained values in the 0.11-0.2 GPa range (0.1 GPa nominal reference value). The Young modulus is obtained by fitting the repulsive part of the force curve to the Hertz contact mechanics model for a sphere with a radius of 15 nm.

Equations (6) and (7) also provide a unified description of amplitude and frequency modulation AFM force reconstruction methods. In both methods the reconstruction involves the sum of three integrals. In AM-AFM the amplitude changes with distance. This is reflected in the existence of a derivative of A in the third integral. In frequency modulation AFM where the amplitude is held constant [24] there is a term that contains a derivative of the frequency shift [25, 48]. The resemblance of the integrals happens despite that the derivation of the equations are based on different mathematical approaches.

The forces involved in amplitude modulation force microscopy measurements have a non-linear dependence with the distance, consequently the tip motion could show some non-linear dynamics features [54]. Those effects as well as the difference observed between the actual and observed tip displacement have not been considered in the force reconstruction method. However, high resolution and non-invasive imaging experiments need to be performed in situations that involve a quasi-harmonic motion. In addition, the transient components have disappeared during the measurements because

the oscillation period in the 10-10^3 kHz range and the amplitude and phase shift curves are acquired in 1-10 Hz range.

VI. CONCLUSION

We have developed a method to reconstruct the force from amplitude modulation (tapping mode) AFM experiments. The two integral equations, in-phase and quadrature, require as experimental inputs the amplitude and phase shift curves. The key technical features of the method are the assumption that the oscillation is a slowly varying function of the probe-surface separation and the use of fractional calculus methods. The force reconstruction method involves three terms, however, for many cases relevant only two terms are needed which makes the final formulas more compact.

We have compared this approach with other force reconstruction methods. The method provides force curves that are closer to the model force. The accuracy and applicability of the method is validated by numerical simulations and experiments. The method is valid for liquid and air environments, small and large amplitudes, compliant and rigid materials, conservative and non-conservative forces. The agreement between the model force and the method is good (relative error below 10%) for amplitudes amounting 0.7 of the free amplitude. It takes a few milliseconds to reconstruct the force curve once the experimental data has been recorded. This force reconstruction method will expand the capabilities of tapping mode AFM to enable a robust, fast and accurate determination of the mechanical properties of soft-matter interfaces.

Acknowledgement. We thank Udo D. Schwarz for his encouraging comments. This work was funded by the Spanish Ministry of Economy (MINECO) through grant CSD2010-00024 and the European Research Council ERC-AdG-340177 (3DNanoMech).

APPENDIX: DEDUCTION OF THE INTEGRAL EQUATIONS

The cantilever-tip motion in amplitude modulation AFM is approximately described by

$$\ddot{z} + \frac{\omega_0}{Q}\dot{z} + \omega_0^2 z = \frac{\omega_0^2 F_{ts}}{k} + \frac{\omega_0^2 F_d}{k} \quad \text{(A1)}$$

we assume a sinusoidal solution,

$$z = z_0 + A\cos(\omega t - \phi) \quad \text{(A2)}$$

where

$$F_{ts} = F_c + F_{nc} = F_c(z_0 + z_c + A\cos(\omega t - \phi)) + \Lambda\big(z_0 + z_c + A\cos(\omega t - \phi)\big)\dot{z} \quad \text{(A3)}$$

$$F_d = \frac{A_0 k}{Q}\cos\omega t \quad \text{(A4)}$$

The key hypothesis is to consider that A and ϕ are slowly varying functions of time when the probe-surface separation distance is changed.

By taking the time derivative of the displacement in equation (A2)

$$\dot{z} = \dot{A}\cos\beta - A\omega\sin\beta + A\dot{\phi}\sin\beta = -A\omega\sin\beta \quad \text{(A5)}$$

where

$$\beta = \omega t - \phi \quad \text{(A6)}$$

from equation (A5) we get

$$\dot{A}\cos\beta = -A\dot{\phi}\sin\beta \quad \text{(A7)}$$

by taking the time derivative in equation (A5), the tip acceleration is obtained

$$\ddot{z} = -\dot{A}\omega\sin\beta - A\omega^2\cos\beta + A\omega\dot{\phi}\cos\beta \quad \text{(A8)}$$

By substituting equations (A5) and (A8) into (A1) and with the assumption that z_0 is much smaller than A we get

$$-\dot{A}\omega\sin\beta - A\omega^2\cos\beta + A\omega\dot{\phi}\cos\beta - \frac{A\omega\omega_0\sin\beta}{Q} + A\omega_0^2\cos\beta = \frac{\omega_0^2}{k}F_{ts} + \frac{\omega_0^2}{k}F_d \quad \text{(A9)}$$

A. Conservative forces

By multiplying equation (A9) by $\cos\beta$ and integrating the resulting equation in one period we obtain (in the steady-state the time derivatives of A and ϕ are zero)

$$\int_0^{2\pi} F_{ts}(z_c + Acos\beta)cos\beta d\beta = \int_0^{2\pi} F_c(z_c + Acos\beta)cos\beta d\beta = -\pi \frac{kA_0}{Q} cos\phi + \pi kA\left(\frac{\omega_0^2-\omega^2}{\omega_0^2}\right) \quad \text{(A10)}$$

We note that the over one period the integrals that involve $cos\beta sin\beta$ are zero.

Now we define the variable

$$u = cos\beta \quad \text{(A11)}$$

Then equation (A10) is transformed into

$$\int_{-1}^{1} F_c\,(z_c + Au)\frac{udu}{\sqrt{1-u^2}} = \int_{-1}^{1} F_c\,(d + A + Au)\frac{udu}{\sqrt{1-u^2}} = -\pi \frac{kA_0}{2Q} cos\phi + \frac{\pi kA}{2}\left(\frac{\omega_0^2-\omega^2}{\omega_0^2}\right) \quad \text{(A12)}$$

To solve the above equation we introduce the definition of the Laplace transform of the force [48]

$$F_c(d) = \int_0^{\infty} F_c(\lambda)\exp(-\lambda d)\,d\lambda \quad \text{(A13)}$$

into equation (A12)

$$\int_{-1}^{1} F_c\,(d + A + Au)\frac{udu}{\sqrt{1-u^2}} = -\pi \int_0^{\infty} F_c(\lambda)T(\lambda A)\exp(-\lambda d)\,d\lambda \quad \text{(A14)}$$

with

$$T(\lambda A) = \int_{-1}^{1} exp\big(-\lambda(A + Au)\big)\frac{u}{\sqrt{1-u^2}}du \quad \text{(A15)}$$

which leads to

$$\int_0^{\infty} F_c(\lambda)T(\lambda A)\exp(-\lambda d)\,d\lambda = \frac{kA_0}{2Q} cos\phi - \frac{kA}{2}\left(\frac{\omega_0^2-\omega^2}{\omega_0^2}\right) \quad \text{(A16)}$$

where $T(\lambda A)$ can be expressed in terms of the modified Bessel function of the first kind of order one $I_1(\lambda A)$

$$T(\lambda A) = I_1(\lambda A)\exp(-\lambda A) \quad \text{(A17)}$$

To facilitate the solution of the above integral, an approximate function is constructed for $T(\lambda A)$ by considering its known asymptotic limits as $\lambda A \to 0$ and $\lambda A \to \infty$ and using the Padé approximant [25]

$$T(\lambda A) \cong \frac{\lambda A}{2}(1 + \alpha\sqrt{\lambda A} + \sqrt{\frac{\pi}{2}}(\lambda A)^{3/2})^{-1} \qquad 0.1 \le \alpha \le 0.4 \tag{A18}$$

where

$$\begin{cases} \lambda A \to 0 & T(\lambda A) = \frac{\lambda A}{2} \\ \lambda A \to \infty & T(\lambda A) = \frac{1}{\sqrt{2\pi\lambda A}} \end{cases} \tag{A19}$$

the exact analytical solution for $F_c(d)$ is

$$F_c(d) = L\left\{\frac{1}{T(\lambda A)} L^{-1}\left\{\frac{kA_0}{2Q}cos\phi - \frac{kA}{2}\left(\frac{\omega_0^2-\omega^2}{\omega_0^2}\right)\right\}\right\} \tag{A20}$$

where the operators L and L^{-1} refer to the Laplace and inverse Laplace transforms, respectively. By defining

$$X = \frac{A_0}{2AQ}cos\phi - \frac{1}{2}\left(\frac{\omega_0^2-\omega^2}{\omega_0^2}\right) \tag{A21}$$

and applying fractional integrals and derivatives as it is done in [49], the conservative force can be calculated as

$$F_c(d) = 2k\left[\int_d^\infty X dx + \alpha\sqrt{A} I_-^{1/2} X + \sqrt{\frac{\pi}{2}} D_-^{1/2} A^{3/2} X\right] \tag{A22}$$

where

$$I_-^{1/2}\Psi(\lambda) = \frac{1}{\Gamma(1/2)}\int_\lambda^\infty \frac{\Psi(t)}{(t-\lambda)^{1/2}} dt \tag{A23}$$

$$D_-^{1/2}\Psi(\lambda) = \frac{-1}{\Gamma(1/2)}\frac{d}{d\lambda}\int_\lambda^\infty \frac{\Psi(t)}{(t-\lambda)^{1/2}} dt \tag{A24}$$

where $\Gamma(n)$is the gamma function.

which gives

$$F_c(d) = 2k\int_d^\infty X\, dx + 2k\int_d^\infty \frac{\alpha\sqrt{A}}{\sqrt{\pi(x-d)}} X\, dx - 2k\frac{\partial}{\partial d}\int_d^\infty \left(\frac{A^{3/2}}{\sqrt{2(x-d)}} X\right) dx \tag{A25}$$

B. Dissipative forces

By multiplying equation (A9) by *sin β* and integrating over one period we obtain

$$\int_0^{2\pi} F_{ts}(z_c + Acos\beta)sin\beta d\beta = \int_0^{2\pi} F_{nc}(z_c + Acos\beta)sin\beta d\beta = -\frac{\pi\omega Ak}{\omega_0 Q} + \pi\frac{kA_0}{Q}sin\phi$$

(26)

We note that the over one period the integrals that involve $cos\beta sin\beta$ are zero.

We consider the following type of non-conservative

$$F_{nc}(d + A + Au) = \Lambda(d + A + Au)\dot{z} = -\Lambda(d + A + Au)A\omega sin\beta \quad \text{(A27)}$$

where $\Lambda(d, A, \omega)$ is a generalized damping coefficient , then

$$\int_0^{2\pi} \Lambda(d + A + Au)A\omega sin^2\beta d\beta = \frac{\pi\omega Ak}{Q\omega_0} - \frac{\pi kA_0}{Q} sin\phi \quad \text{(A28)}$$

Now we use the change of variable given in equation (A11)

$$\int_{-1}^{1} \Lambda(d + A + Au)\sqrt{1 - u^2}du = \frac{\pi k}{2Q\omega_0} - \frac{\pi kA_0}{2QA\omega} sin\phi \quad \text{(A29)}$$

Equation (A29) can be transformed using integration by parts into

$$\int_{-1}^{1} B(d + A + Au)\frac{u}{\sqrt{1-u^2}}du = \frac{\pi kA}{2Q\omega_0} - \frac{\pi kA_0}{2Q\omega} sin\phi \quad \text{(A30)}$$

where we have introduced two intermediate functions

$$p = \sqrt{1 - u^2} \quad \text{(A31)}$$

$$B(x) = 2\int_x^{\infty} \Lambda(x)dx \quad \text{(A32)}$$

To solve the above equation we introduce the definition of the Laplace transform of *B*

$$B(d) = \int_0^{\infty} B(\lambda)\exp(-\lambda d)\, d\lambda \quad \text{(A33)}$$

into equation (A30)

$$\int_{-1}^{1} B\,(d + A + Au)\frac{udu}{\sqrt{1-u^2}} = -\pi\int_0^{\infty} B(\lambda)T(\lambda A)\exp(-\lambda d)\, d\lambda \quad \text{(A34)}$$

with

$$T(\lambda A) = \int_{-1}^{1} exp\big(-\lambda(A + Au)\big)\frac{u}{\sqrt{1-u^2}}du \quad \text{(A35)}$$

which leads to

$$\int_0^{\infty} B(\lambda)T(\lambda A)\exp(-\lambda d)\, d\lambda = -\frac{Ak}{2Q\omega_0} + \frac{kA_0}{2Q\omega} sin\phi \quad \text{(A36)}$$

where $T(\lambda A)$ can be expressed in terms of the modified Bessel function of the first kind of order one $I_1(\lambda A)$

$$T(\lambda A) = I_1(\lambda A)\exp(-\lambda A) \tag{A37}$$

To facilitate the solution of the above integral, an approximate function is constructed for $T(\lambda A)$ by considering its known asymptotic limits as $\lambda A \to 0$ and $\lambda A \to \infty$ and using Padé approximant [25]

$$T(\lambda A) \cong \frac{\lambda A}{2}(1 + \alpha\sqrt{\lambda A} + \sqrt{\frac{\pi}{2}}(\lambda A)^{3/2})^{-1} \qquad 0.1 \le \alpha \le 0.4 \tag{A38}$$

where

$$\begin{cases} \lambda A \to 0 & T(\lambda A) = \frac{\lambda A}{2} \\ \lambda A \to \infty & T(\lambda A) = \frac{1}{\sqrt{2\pi\lambda A}} \end{cases} \tag{A39}$$

the exact analytical solution for $B(d)$ is

$$B(d) = L\left\{\frac{1}{T(\lambda A)}L^{-1}\left\{-\frac{kA}{2\omega_0 Q} + \frac{kA_0}{2\omega Q}sin\phi\right\}\right\} \tag{A40}$$

by defining

$$Y = \frac{A_0}{2QA\omega}sin\phi - \frac{1}{2Q\omega_0} \tag{A41}$$

and applying the fractional integrals and derivatives as it is done in [49], the damping coefficient is given by

$$\Lambda(d) = 2k\frac{\partial}{\partial d}\left[\int_{\mathrm{d}}^{\infty}\mathrm{Ydx} + \alpha\sqrt{A}I_{-}^{1/2}Y + \sqrt{\frac{\pi}{2}}D_{-}^{1/2}A^{3/2}Y\right] \tag{A42}$$

which gives

$$\Lambda(d) = 2k\frac{\partial}{\partial d}\int_d^{\infty}Ydx + 2k\frac{\partial}{\partial d}\int_d^{\infty}\frac{\alpha\sqrt{A}}{\sqrt{\pi(x-d)}}Ydx - 2k\frac{\partial^2}{\partial d^2}\int_d^{\infty}\frac{A^{3/2}}{\sqrt{2(x-d)}}Y\,dx \tag{A43}$$

References

[1] Binnig G, Quate C F and Gerber C 1986 Atomic Force Microscope *Phys. Rev. Lett.* **56** 930-933

[2] Barth C, Foster A S, Henry C R and Shluger A L 2011 Chemistry with High-Resolution Scanning Force Methods *Adv. Mater.* **23** 477-501

[3] Gan Y 2009 Atomic and Subnanometer Resolution in Ambient Conditions by Atomic Force Microscopy *Surface Sci. Rep.* **64** 99-121

[4] Kodera N, Yamamoto D, Ishikawa R and Ando T 2010 Video Imaging of Walking Myosin V by High-Speed Atomic Force Microscopy *Nature* **468** 72-76

[5] Casuso I, Khao J, Chami M, Paul-Gilloteaux P, Husain M, Duneau J P, Stahlberg H, Sturagis J N and Scheuring S 2012 Characterization of the Motion of Membrane Proteins Using High-Speed Atomic Force Microscopy *Nat. Nanotechnol.* **7** 525-529

[6] Herruzo E T, Asakawa H, Fukuma T and Garcia R 2013 Three-Dimensional Quantitative Force Maps in Liquid with 10 Piconewton, Angstrom and Sub-Minute Resolutions *Nanoscale* **5** 2678-2685

[7] Ido S, Kimura K, Oyabu N, Kobayashi K, Tsukada M, Matsushige K and Yamada H 2013 Beyond the Helix Pitch: Direct Visualization of Native DNA in Aqueous Solution *Acs Nano* **7** 1817-1822

[8] Sugimoto Y, Pou P, Abe M, Jelinek P, Perez R, Morita S and Custance O 2007 Chemical Identification of Individual Surface Atoms by Atomic Force Microscopy *Nature* **446** 64-67

[9] Rico F, Su C M and Scheuring S 2011 Mechanical Mapping of Single Membrane Proteins at Submolecular Resolution *Nano Lett.* **11** 3983-3986

[10] Voitchovsky K, Kuna J J, Contera S A, Tosatti E and Stellacci F 2010 Direct Mapping of the Solid-Liquid Adhesion Energy with Subnanometre Resolution *Nat. Nanotechnol.* **5** 401-405.

[11] Raman A,Trigueros S, Cartagena A, Stevenson A P Z, Susilo M, Nauman E and Contera S A 2011 Mapping Nanomechanical Properties of Live Cells Using Multi-Harmonic Atomic Force Microscopy *Nat. Nanotechnol.* **6** 809-814

[12] Martinez-Martin D, Herruzo E T, Dietz C, Gomez-Herrero J and Garcia R 2011 Noninvasive Protein Structural Flexibility Mapping by Bimodal Dynamic Force Microscopy *Phys. Rev. Lett.* **106** 4

[13] Dokukin M E and Sokolov I 2012 Quantitative Mapping of the Elastic Modulus of Soft Materials with HarmoniX and Peak Force QNM AFM Modes *Langmuir* **28** 16060-16071

[14] Dufrene Y F, Martinez-Martin D, Medalsy I, Alsteens D and Muller D J 2013 Multiparametric Imaging of Biological Systems by Force-Distance Curve-Based AFM *Nat. Methods* **10** 847-854

[15] Ebeling D, Eslami B and Solares S D 2013 Visualizing the Subsurface of Soft Matter: Simultaneous Topographical Imaging, Depth Modulation, and Compositional Mapping with Triple Frequency Atomic Force Microscopy *ACS Nano* **7** 10387-10396

[16] Hernando-Perez M, Miranda R, Aznar M, Carrascosa J L, Schaap I A, Requera D and de Pablo P J 2012 Direct Measurement of Phage phi29 Stiffness Provides Evidence of Internal Pressure *Small* **8** 2366-2370

[17] Chyasnavichyus M, Young S L and Tsukruk V V 2014 Probing of Polymer Surfaces in the Viscoelastic Regime *Langmuir* doi.org/10.1021/la404925h

[18] Goetz J G et al 2011 Biomechanical Remodeling of the Microenvironment by Stromal Caveolin-1 Favors Tumor Invasion and Metastasis *Cell* **146** 148-163
[19] Butt H J, Capella B and Kappl M 2005 Force Measurements with the Atomic Force Microscope: Technique, Interpretation and Applications *Surf. Sci. Rep.* **59** 1-152
[20] Garcia R and San Paulo A 1999 Attractive and Repulsive Tip-Sample Interaction Regimes in Tapping-Mode Atomic Force Microscopy *Phys. Rev. B* **60** 4961-4967
[21] Garcia R, Gomez C J, Martinez N F, Patil S, Dietz C and Magrele R 2006 Identification of Nanoscale Dissipation Processes by Dynamic Atomic Force Microscopy *Phys. Rev. Lett.* **97** 016103
[22] Jesse S, Kalinin S V, Proksch R, Baddorf A P and Rodriguez B J 2007 The Band Excitation Method in Scanning Probe Microscopy for Rapid Mapping of Energy Dissipation on the Nanoscale *Nanotechnology* **18** 435503
[23] Attard P 2007 Measurement and Interpretation of Elastic and Viscoelastic Properties with the Atomic Force Microscope *J. Phys.: Condens. Matter*. **19** 473201
[24] Giessibl F J 2003 Advances in Atomic Force Microscopy *Rev. Mod. Phys.* **75** 949
[25] Sader J E, Uchihashi T, Higgins M J, Farrel A, Nakayama Y and Jarvis S P 2005 Quantitative Force Measurements Using Frequency Modulation Atomic Force Microscopy - Theoretical Foundations *Nanotechnology* **16** S94-S101
[26] Forchheimer D, Platz D, Tholen E A and Haviland D B 2012 Model-Based Extraction of Material Properties in Multifrequency Atomic Force Microscopy *Phys. Rev. B* **85** 7
[27] Platz D, Forchheimer D, Tholen E A and Haviland D B 2013 Polynomial Force Approximations and Multifrequency Atomic Force Microscopy *Beilstein J. Nanotechnol.* **4** 352-360
[28] Saraswat G, Agarwal P, Haugstad G and Salapaka M V 2013 Real-Time Probe Based Quantitative Determination of Material Properties at the Nanoscale *Nanotechnology* **24** 12.
[29] Santos S, Gadelrab K, Font J and Chiesa M 2013 Single-Cycle Atomic Force Microscope Force Reconstruction: Resolving Time-Dependent Interactions *New J Phys.* **15** 20
[30] Guzman H V, Perrino A P and Garcia R 2013 Peak Forces in High-Resolution Imaging of Soft Matter in Liquid *ACS Nano* **7** 3198-3204
[31] Solares S D, Chang J, Seong J and Kareem A U 2011 Utilization of Simple Scaling Laws for Modulating Tip-Sample Peak Forces in Atomic Force Microscopy Characterization in Liquid Environments *J. Appl. Phys.* **110** 094904
[32] Vandat V and Carpick R W 2013 Practical Method to Limit Tip-Sample Contact Stress and Prevent Wear in Amplitude Modulation Atomic Force Microscopy *ACS Nano* **7** 9836-9850
[33] Hölscher H and Schwarz U D 2007 Theory of Amplitude Modulation Atomic Force Microscopy with and without Q-Control *Int. J. Nonlin. Mech.* **42** 608-625
[34] Legleiter J, Park M, Cusick B and Kowalewski T 2006 Scanning Probe Acceleration Microscopy (SPAM) in Fluids: Mapping Mechanical Properties of Surfaces at the Nanoscale *Proc. Natl. Acad. Sci. USA* **103** 4813-4818
[35] Shamitko-Klingensmith N, Molchanoff K M, Burke K A, Magnone G J and Legleiter J 2012 Mapping the Mechanical Properties of Cholesterol-Containing Supported Lipid Bilayers with Nanoscale Spatial Resolution *Langmuir* **28** 13411-13422

[36] Stark M, Stark R W, Heckl W M and Guckenberger R 2002 Inverting Dynamic Force Microscopy: From Signals to Time-Resolved Interaction Forces *Proc. Natl. Acad. Sci. USA* **99** 8473-8478
[37] Sahin O, Magonov S, Su C, Quate C F and Solgaard O 2007 An Atomic Force Microscope Tip Designed to Measure Time-Varying Nanomechanical Forces *Nat. Nanotechnol.* **2** 507-514
[38] Holscher H 2006 Quantitative Measurement of Tip-Sample Interactions in Amplitude Modulation Atomic Force Microscopy *Appl. Phys. Lett.* **89** 3
[39] Lee M H and Jhe W H 2006 General Theory of Amplitude-Modulation Atomic Force Microscopy *Phys. Rev. Lett.* **97** 4
[40] Hu S Q and Raman A 2008 Inverting Amplitude and Phase to Reconstruct Tip-Sample Interaction Forces in Tapping Mode Atomic Force Microscopy *Nanotechnology* **19** 11
[41] Katan A J, van Es M H and Oosterkamp T H 2009 Quantitative Force Versus Distance Measurements in Amplitude Modulation AFM: a Novel Force Inversion Technique *Nanotechnology* **20** 9
[42] Dong M D and Sahin O A 2011 Nanomechanical Interface to Rapid Single-Molecule Interactions *Nat. Commun.* **2** 6
[43] Dong M, Husale S and Sahin O 2009 Determination of Protein Structural Flexibility by Microsecond Force Spectroscopy *Nat. Nanotechnol.* **4** 514-517
[44] Platz D, Forchheimer D, Tholen E A and Haviland D B 2013 Interpreting Motion and Force for Narrow-Band Intermodulation Atomic Force Microscopy *Beilstein J. Nanotechnol.* **4** 45-56
[45] Lozano J R and Garcia R 2009 Theory of Phase Spectroscopy in Bimodal Atomic Force Microscopy *Phys. Rev. B* **79** 9
[46] H. Holscher, Ch. 2, in Dynamic Force Spectroscopy and Biomolecular Recognition, CRC Press, 2012
[47] Platz D. Forchheimer, D., Tholen, E. A., Haviland D.B 2012. Interaction imaging with amplitude-dependence force spectroscopy *Nat. Commun.* **4** 1360
[48] Sader J E and Jarvis S P 2004 Accurate Formulas for Interaction Force and Energy in Frequency Modulation Force Spectroscopy *Appl. Phys. Lett.* **84** 1801-1803
[49] Herruzo E T and Garcia R 2012 Theoretical Study of the Frequency Shift in Bimodal FM-AFM by Fractional Calculus Beilstein J. Nanotechnol. 3 198-206
[50] Sinha A 2005 Nonlinear Dynamics of Atomic Force Microscope with PI Feedback J. Sound Vib. **288** 387-394
[51] Melcher J, Martinez-Martin D, Jaafar M, Gomez-Herrero J and Raman A 2013 High-Resolution Dynamic Atomic Force Microscopy in Liquids with Different Feedback Architectures *Beilstein J. Nanotechnol.* **4** 153-163
[52] Rodriguez T R and Garcia R 2004 Compositional mapping of surfaces in atomic force microscopy by excitation of the second normal mode of the microcantilever Appl. Phys. Lett. 84 449-451
[53] Herruzo E T, Perrino A P and Garcia R 2014 Fast nanomechanical spectroscopy of soft matter *Nat. Commun.* **5** 3126
[54] Kiracofe D and Raman A 2012 Nonlinear Dynamics of the Atomic Force Microscope at the Liquid-Solid Interface *Phys. Rev. B* **86** 16

Figure Captions

FIG. 1. Scheme of distances and observables in tapping mode AFM. (a) The amplitude and phase shift are the observables to obtain the force curve. (b) z is the instantaneous tip deflection; z_c is the probe-sample separation; d is the tip closest approach to the sample surface (it can have negative values); z_0 is the average tip deflection. In the scheme it is depicted a case where the average force is negative (attractive regime), then z_0 is below the equilibrium position of the cantilever in the absence of any force. When the tip deflection is negligible with respect to the A, z_c coincides with the average tip-surface distance.

FIG. 2. Conservative force reconstruction for a rigid material (10 GPa) in air and water (simulations). (a) Amplitude and phase shift *versus* probe-surface separation (air). (b) Amplitude and phase shift *versus* tip-surface distance (air). (c) Comparison between the interaction force (model) and the reconstructed force by using equation (6) (air). (d) Amplitude and phase shift *versus* probe-surface separation (water). e, Amplitude and phase shift *versus* tip-surface distance (water). (f) Comparison between the interaction force (model) and the reconstructed force by using equation (6) (water).

FIG. 3. Conservative force reconstruction for a compliant material (100 MPa) in air and water (simulations). (a) Amplitude and phase shift *versus* probe-surface separation (air). (b) Amplitude and phase shift *versus* tip-surface distance (air). (c) Comparison between the interaction force (model) and the reconstructed force by using equation (6) (air). (d) Amplitude and phase shift *versus* probe-surface separation (water). (e) Amplitude and phase shift *versus* tip-surface distance (water). (f) Comparison between the interaction force (model) and the reconstructed force by using equation (6) (water).

FIG. 4. Comparison among the different force reconstruction terms (conservative forces). (a) Total force and contributions from the different terms of equation (6a) (air). (b) Total force and contributions from the different integrals of equation (6a) (water). (c) Comparison among different force reconstruction models (air). (d) Comparison among different force reconstruction models (water).

FIG. 5. Comparison among different force reconstruction terms (dissipation). (a) Contributions of the different terms of equation (7a) to the dissipative coefficient (air). (b) Contributions of the different terms of equation (7a) to the dissipative coefficient (water). (c) Comparison between the reconstructed dissipative coefficient and the model (air). (d) Comparison between the reconstructed dissipative coefficient and the model (water).

FIG. 6. Force reconstruction (conservative) on polymer surfaces. (a) AFM image of a PS-LDPE polymer blend . The crosses indicate the positions where the data have been acquired. (b) Amplitude and phase shift versus z-piezo displacement (z_c, probe-surface separation). (c) Minimum distance *versus* z_c. (d) Amplitude *versus* tip-surface distance. (e) Tip-surface force reconstruction on PS (air). (f) Amplitude and phase shift versus z-piezo displacement. (g) Minimum distance *versus* z_c. (h) Amplitude *versus* tip-surface

distance. (i) Tip-surface force reconstruction on LDPE (air). (j) AFM image of a PS region in water. (k) Amplitude and phase shift *versus* z_c. (l) Minimum distance *versus* z_c. (m) Amplitude *versus* tip-surface distance. (n) Tip-surface force reconstruction for PS (water).

Figure 1

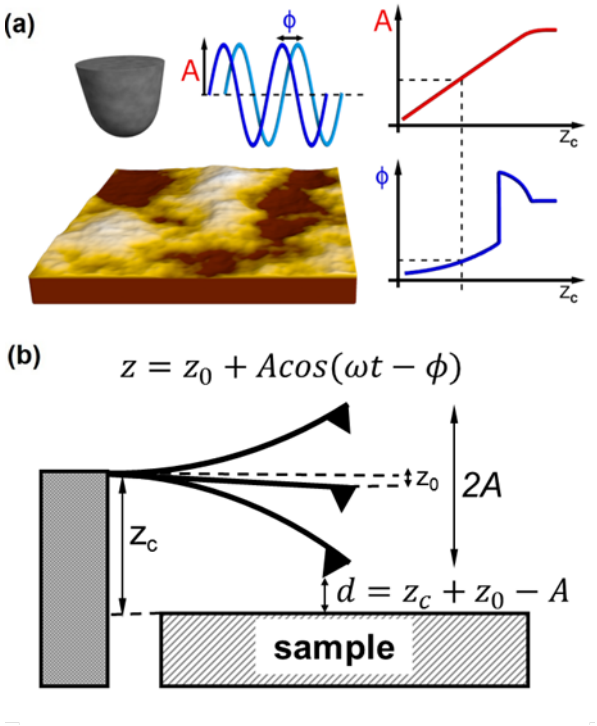

Figure 2

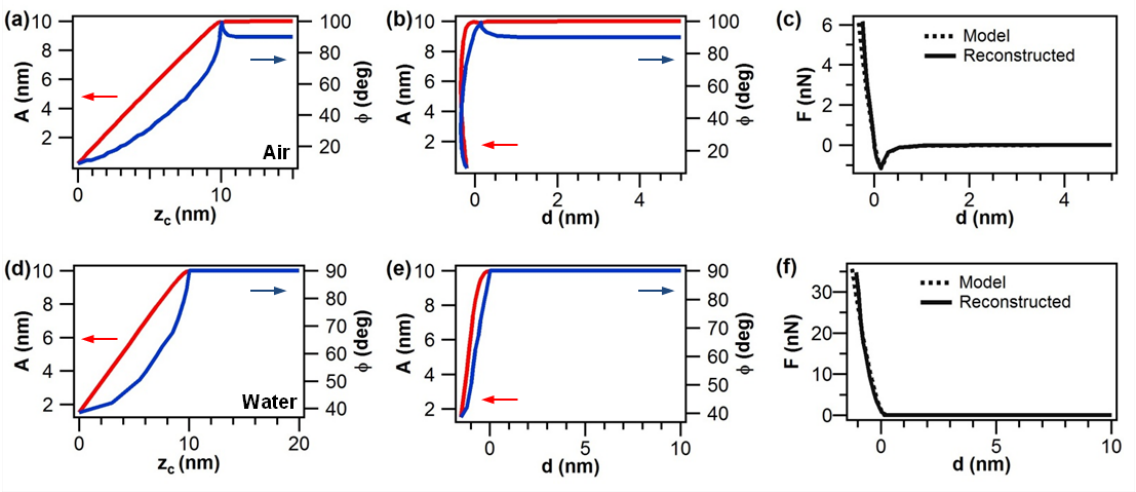
(a)
A (nm)
ϕ (deg)
Air
z_c (nm)
(b)
A (nm)
ϕ (deg)
d (nm)
(c)
Model
Reconstructed
F (nN)
d (nm)
(d)
A (nm)
ϕ (deg)
Water
z_c (nm)
(e)
A (nm)
ϕ (deg)
d (nm)
(f)
Model
Reconstructed
F (nN)
d (nm)

Figure 3

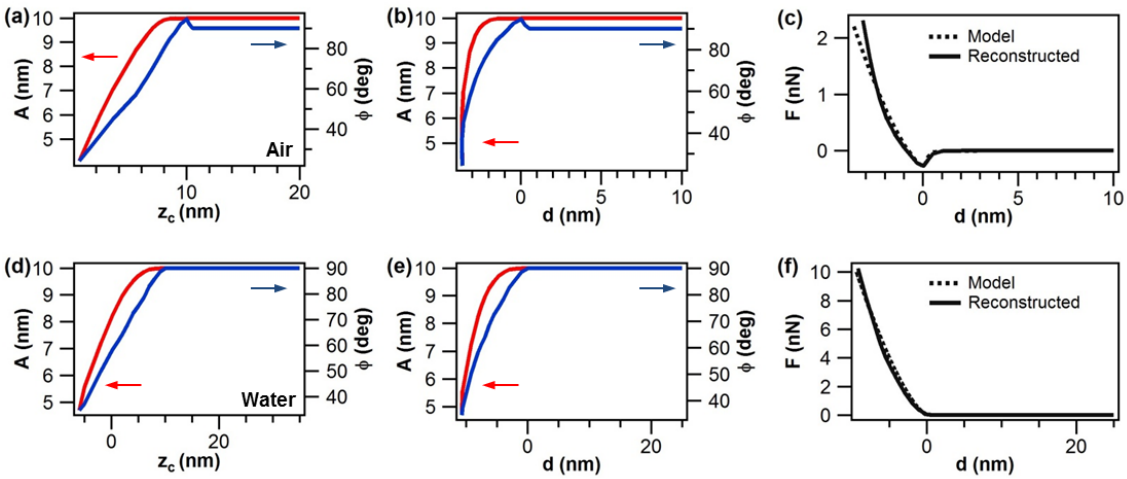
(a)
A (nm)
ϕ (deg)
Air
z_c (nm)
(b)
A (nm)
ϕ (deg)
d (nm)
(c)
F (nN)
Model
Reconstructed
d (nm)
(d)
A (nm)
ϕ (deg)
Water
z_c (nm)
(e)
A (nm)
ϕ (deg)
d (nm)
(f)
F (nN)
Model
Reconstructed
d (nm)

Figure 4

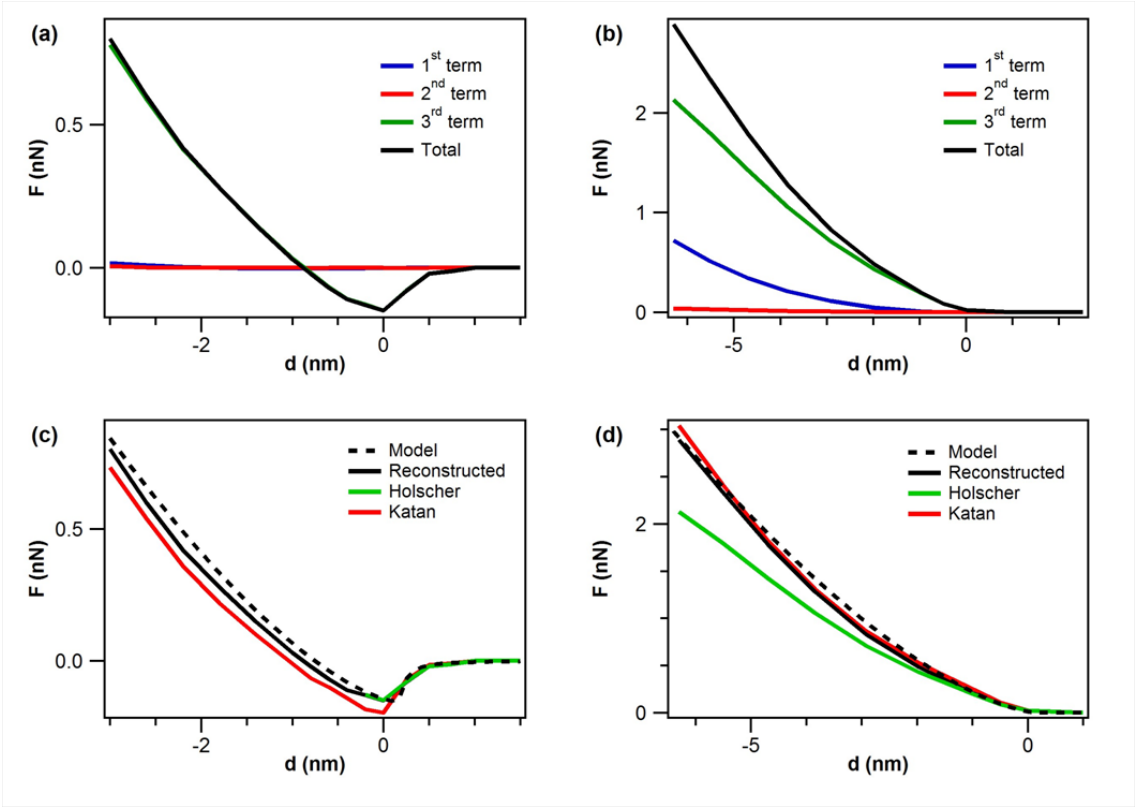
(a)
1st term
2nd term
3rd term
Total
F (nN)
d (nm)
(b)
1st term
2nd term
3rd term
Total
F (nN)
d (nm)
(c)
Model
Reconstructed
Holscher
Katan
F (nN)
d (nm)
(d)
Model
Reconstructed
Holscher
Katan
F (nN)
d (nm)

Figure 5

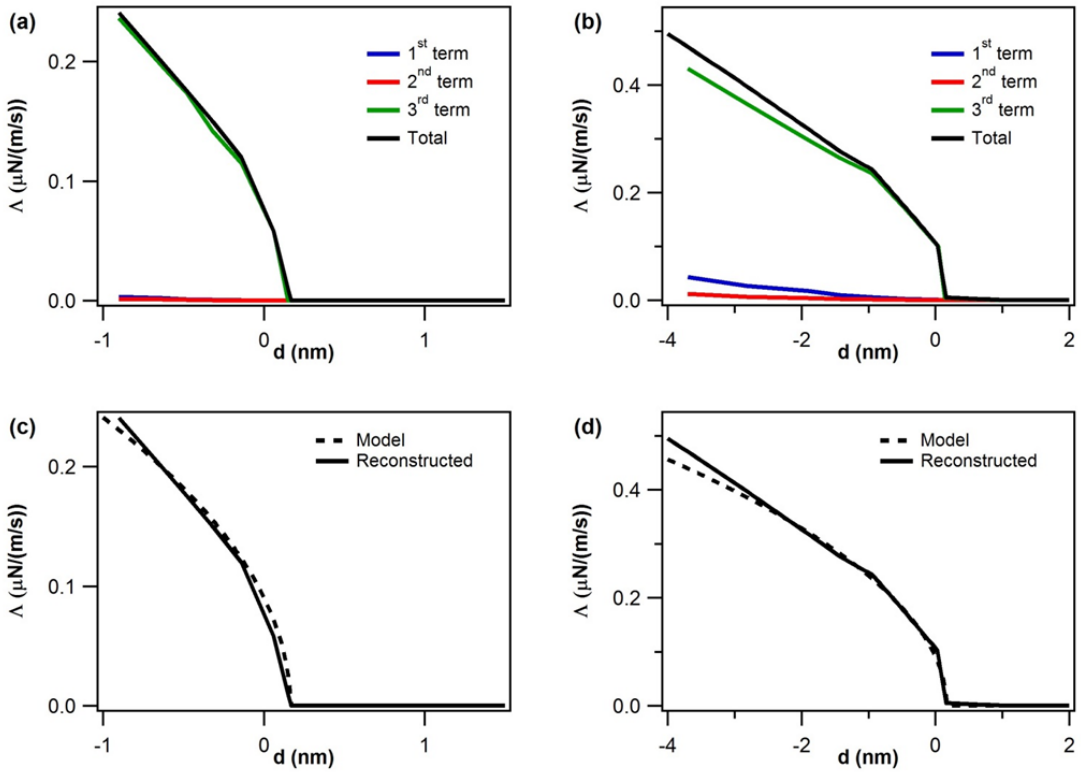
(a)
1st term
2nd term
3rd term
Total
Λ (μN/(m/s))
d (nm)
(b)
1st term
2nd term
3rd term
Total
Λ (μN/(m/s))
d (nm)
(c)
Model
Reconstructed
Λ (μN/(m/s))
d (nm)
(d)
Model
Reconstructed
Λ (μN/(m/s))
d (nm)

Figure 6

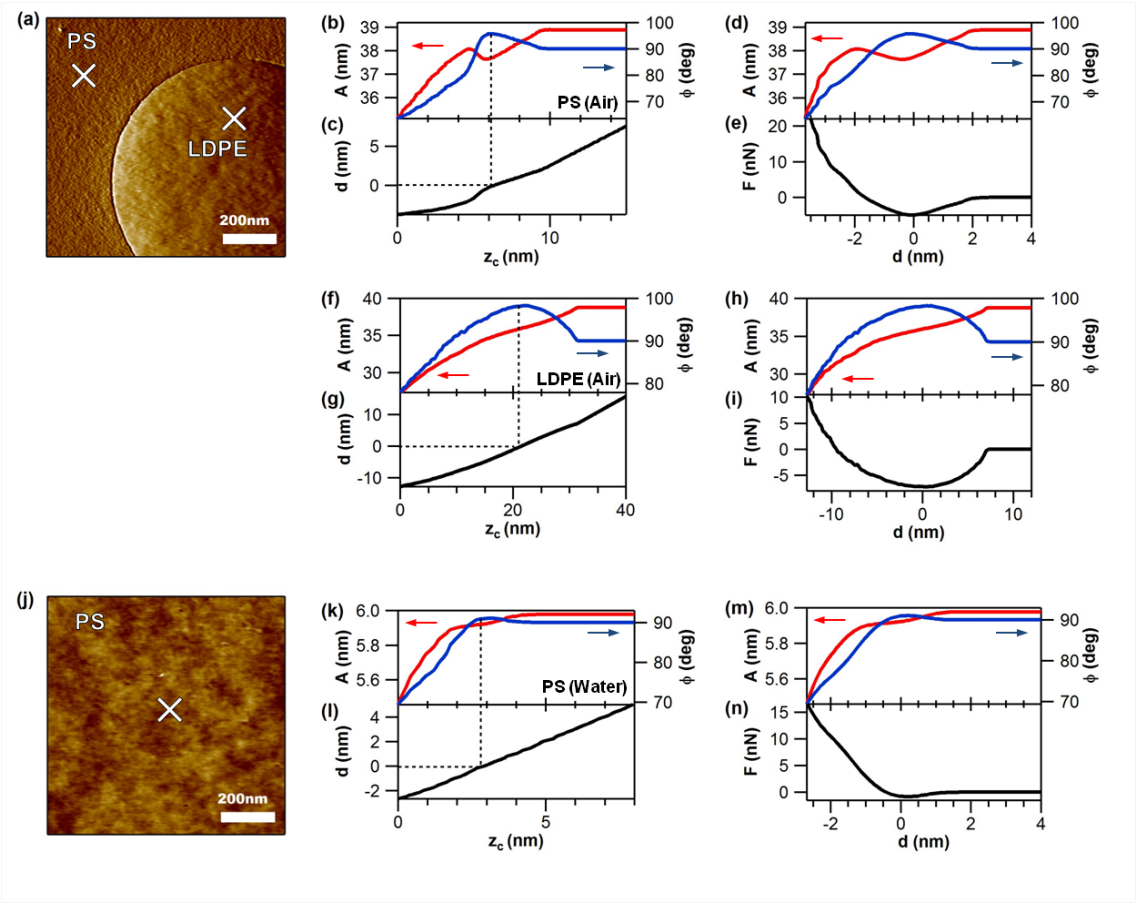
(a)
PS
LDPE
200nm
(b)
A (nm)
ϕ (deg)
PS (Air)
(c)
d (nm)
z_c (nm)
(d)
(e)
F (nN)
d (nm)
(f)
LDPE (Air)
(g)
(h)
(i)
(j)
PS
200nm
(k)
PS (Water)
(l)
(m)
(n)